Dynamic SAXS Studies of Sphere-Forming Block Copolymers under Large Oscillatory Shear Deformation†

Shigeru Okamoto,‡ Kenji Saijo, and Takeji Hashimoto*

Division of Polymer Chemistry, Graduate School of Engineering, Kyoto University, Kyoto 606, Japan

Received December 21, 1993; Revised Manuscript Received April 18, 1994®

ABSTRACT: Rheo-optical studies were conducted on a polystyrene-*block*-poly(ethylene-*alt*-propylene) copolymer having spherical microdomains composed of polystyrene block chains in a matrix composed of poly(ethylene-*alt*-propylene) block chains. Small-angle X-ray scattering (SAXS) was detected with a 2D detector simultaneously with stress measurements on specimens subjected to a large-amplitude oscillatory shear deformation with a strain amplitude of 50% and a zero static strain at a frequency of 0.0936 rad/s and at room temperature, with the purpose to elucidate a relationship between macroscopic properties of the systems and their mesoscopic structure as revealed by SAXS. The results indicated that the spheres are packed in a body-centered-cubic (bcc) lattice with a large paracrystal distortion and that the shear deformation induces a preferential orientation of (110) lattice planes parallel to the *Oxy* plane and the elastic deformation of the bcc lattice under this particular (110) lattice plane orientation. Here *Oy* is parallel to the direction of the shear displacement vector and *Oyz* is the plane in which the shear strain exists. The stress amplitude $\sigma(N)$ is found to decay with N, the number of strain cycle, and the stress decay to be recovered after cessation of shear. The stress decay with N and the stress recovery after the cessation appear to be interrelated to the preferential orientation of the (110) plane with N and its orientation relaxation after the cessation, respectively. The change of the elastic strain amplitude on the lattice with N and with time after cessation of shear was also proposed to be responsible for the stress decay and stress recovery.

I. Introduction

We explored a relationship between the ordered structure in the block copolymer solutions and their rheological behavior by measuring separately small-angle X-ray scattering (SAXS) and rheology on the same solutions.[1] The solutions studied were a polystyrene-*block*-polybutadiene (SB) in a solvent of *n*-tetradecane (C14), selectively good for polybutadiene block chains (PB) but very poor for polystyrene chains (PS). They formed the spheres composed of PS in the matrix of the PB chains swollen with C14. The junction points between the two block chains are preferentially located at the interfaces between the spheres and the matrix. The SAXS studies revealed that at low temperatures and/or high concentrations the spherical microdomains are packed in a cubic lattice with a long-range order. This ordered structure was found to give rise to a linear viscoelastic property with shear modulus G, if shear stress σ is smaller than the yield stress σ_0 of the solutions, or a nonlinear, plastic flow, if $\sigma > \sigma_0$. Both σ_0 and G were found to be proportional to polymer concentration ϕ_p, which in turn was explained in terms of entropy elasticity of the confined chains, i.e., the elasticity of the swollen PB chains emanating from the vitrified PS spheres.

When the cubic lattice is deformed as shown in Figure 1a, b, the end-to-end vectors $\mathbf{r}_1$ and $\mathbf{r}_2$ of the PB block chains are deformed to $\mathbf{r}_1'$ and $\mathbf{r}_2'$, respectively, to satisfy the demand of the uniform space filling by the corona chains (the block chains emanating from the spheres), as a consequence of low osmotic compressibility of the solution at high concentrations. The elastic deformation of the polymer coils leads to a decrease of the conformational entropy of the confined chains and hence an increase in elastic free energy. In this way the excess free energy $\delta\Delta G$ is stored in the system as shown in Figure 1c, which are responsible for σ_0 and G of the systems. The entropy elasticity of the confined chain was found to give also a nice correlation between the microstructural properties $\delta s/s_m$ and the rheological properties k_BT/GV_c and k_BT/σ_0V_c, where $\delta s/s_m$ is the full width at half-maximum (fwhm) for the first-order SAXS peak relative to its peak position and V_c is the volume of the unit cell.[1]

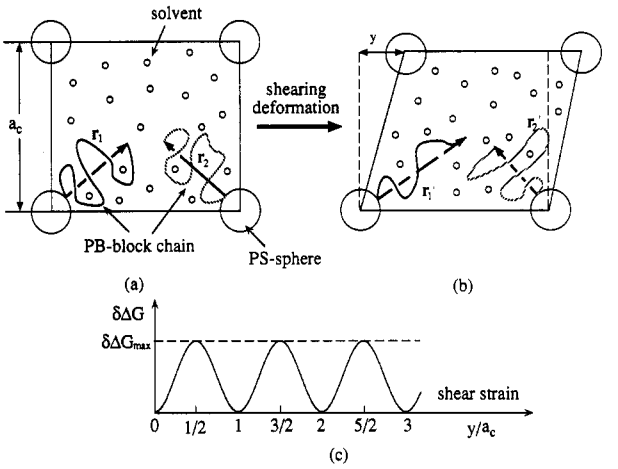

Figure 1. Schematic diagram showing elastic deformation of a cubic lattice formed by microphase-separated block copolymer solutions: (a) undeformed state, (b) deformed state with shear strain $\gamma = y/a_c$, a_c being the length of the cell, and (c) free energy change $\delta\Delta G$ as a function of the shear strain γ (based on ref 1).

In this work we extend our earlier work on the SB/C14 systems to polystyrene-*block*-poly(ethylene-*alt*-propylene) (SEP) in bulk which has a microdomain morphology of spheres composed of PS packed in a bcc lattice with a large paracrystal distortion of the second kind[2,3] in the matrix composed of poly(ethylene-*alt*-propylene) (PEP). We simultaneously observe *in-situ* SAXS and stress for

* To whom correspondence should be addressed.

† Presented in part at the 40th annual meeting of the Society of Polymer Science, Okayama, Japan, Nov 1991 (*Polym. Prepr. Jpn., Soc. Polym. Sci. Jpn.* **1991**, *40*, No. 10, 4035–4037) and at the 42nd annual meeting of the Society of Polymer Science, Kyoto, Japan, May 1993 (*Polym. Prepr. Jpn., Soc. Polym. Sci. Jpn.* **1993**, *42*, No. 4, 1562).

‡ Present address: Department of Materials Science and Engineering, Nagoya Institute of Technology, Nagoya 466, Japan.

® Abstract published in *Advance ACS Abstracts*, June 1, 1994.

0024-9297/94/2227-3753$04.50/0

the specimen subjected to a large oscillatory shear strain in order to investigate a relationship between the deformation behavior of the bcc lattice system and nonlinear mechanical properties.

Almdal et al.[4] reported very interesting results on the effects of large-amplitude oscillatory strain (100% strain with $\omega = 0.02$ rad/s) on the spheres packed in a bcc lattice in the PEP–PEE diblock copolymers. They studied the shear effect at temperatures 70–90 °C, relatively close to the order–disorder transition temperature, $T_{ODT} = 105 \pm 5$ °C, in which both the matrix phase and the sphere phase are far above their glass transition temperatures. In contrast, we study here the shear effect at a frequency $\omega = 0.0936$ rad/s and at temperature $T = 25$ °C; they were respectively higher and much lower than those used by Almdal et al. Our system is far below T_{ODT}, which is estimated[5] to be 180 ± 5 °C by SAXS, and our PS spheres are vitrified in the molten matrix of PEP. Thus we study the shear effects at a very low temperature and a high frequency, i.e., in a regime which is very different from that studied by Almdal et al. The fact that our dispersed phase is vitrified may result in the shear effects which are different also from those studied by simulations and theories.[6,7] It may give rise to some similarities between the behaviors of our system and those of colloidal crystals or of the micellar solution.[8] However, detailed discussions on similarities and dissimilarities are beyond the scope of this study. Here we report some initial results of our studies.

II. Experimental Methods

A. Specimen. SEP which was prepared by selective hydrogenation of a polyisoprene block of polystyrene-*block*-polyisoprene (SI) precursor diblock copolymers was kindly supplied from Kurare Co. Ltd., Japan. It has number-average molecular weight $\bar{M}_n = 3.4 \times 10^4$, heterogeneity index $\bar{M}_w/\bar{M}_n = 1.3$, where $\bar{M}_w$ is weight-average molecular weight, and PS volume fraction in the copolymer (f_{PS}) = 0.103. The polyisoprene block chain had a microstructure rich in 1,4-linkage (95%) before hydrogenation. The as-received SEP specimen which is a viscoelastic liquid at room temperature was annealed under vacuum at 60 °C for 1 week before use for our experiment.

B. Rheo-Optical Method. Simultaneous SAXS and stress measurements were performed by the dynamic SAXS apparatus constructed in our laboratory, the basic part of which was reported previously.[9,10] It is comprised of a 12-kW rotating-anode X-ray generator (operated at 50 kV and 200 mA) and about a 1.7-m SAXS camera with pinhole-collimation optics (two pinholes with 0.5-mm diameter), as shown in Figure 2a. In this work we used the imaging plate system as a 2D detector system.[11] The shear deformation was imposed by a hydraulic deformation apparatus as shown schematically in Figure 2b. The Cu Kα radiation (λ = 1.54 Å) monochromatized with a flat graphite crystal was used as an incident X-ray beam. Two pairs of guard slits parallel to Oy and Oz axes were placed in between the sample position and the second pinhole but close to the sample as much as possible, to avoid parasitic scattering from the second pinhole. Details on the computer-controlled data acquisitions and machine operations were given elsewhere,[10] except for a big change encountered by replacing the 1D position-sensitive proportional counter previously used with the 2D imaging plate. The 2D detector which utilized IP was designed in our laboratory and is now commercially available as a product DIP-220, through MAC Science Co., Ltd., Japan. Details of the apparatus and the data acquisition will be reported elsewhere.[11]

The oscillatory shear strain was imposed on the specimen, sandwiched between two glass plates. As shown in Figure 2b, the incident X-ray beam was irradiated normal to the plane *Oyz* in which the shear strain $\gamma = dy/dz$ exists. The *Oy* axis is the direction parallel to the shear displacement. The SAXS intensity distribution was detected by IP placed normal to the incident beam.

In this work we imposed a large-amplitude sinusoidal shear strain with amplitude $\gamma_0 = 50\%$ and static strain $\gamma_s = 0\%$ and

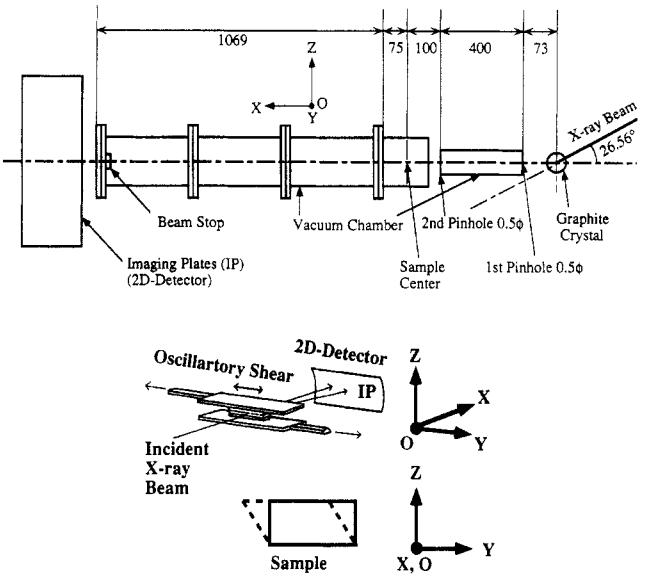

Figure 2. (a) SAXS optical system (in the upper panel); (b) shear deformation driven by a hydraulic deformation device, and the Cartesian coordinate used in this work (in the lower panel). The shear device in part b is set in the sample center in part a. The *Ox* axis is parallel to the propagation direction of the incident beam and to the neutral axis of the shear deformation, the *Oy* axis to the shear displacement direction, and the *Oz* axis to the displacement gradient direction (shear strain exists in the *Oyz* plane).

angular frequency $\omega = 0.0936$ rad/s at 25 °C. The SAXS patterns were taken *in-situ* during oscillatory deformation with the 2D detector. The following two modes were used: (i) the patterns were cumulated onto the detector over many cycles of oscillations between the Nth and $(N + \Delta N)$th cycle, with both N and ΔN being varied (designated hereafter the "average mode" for the sake of convenience), and (ii) the patterns were cumulated at particular strain phases over many cycles of oscillations, between Nth and $(N + \Delta N)$th, in order to count a sufficient number of scattered X-ray photons for good statistical accuracy (designated hereafter the "synchronous mode"). Our IP detector has an octagon shape,[11] each face of which has an IP having area of 100 × 200 mm. The detector plane can be shifted from one face to another by rotating the octagon around its axis. In the synchronous mode, we assigned the four faces of the octagon to the four different phase intervals of the strain and changed these faces in synchronization with the strain phase.

The patterns were also taken as a function of time after cessation of the shear deformation. The change of linear dynamic mechanical response with N during the large-amplitude oscillatory deformation was investigated separately by an RMS605 mechanical spectrometer, Rheometrics Co. Ltd., Piscataway, NJ, under the same conditions as those employed in our rheo-optical experiments. For this purpose a small strain amplitude of $\gamma_0 = 5\%$ and $\gamma_s = 0\%$ were used with parallel-plate geometry, and the real and imaginary parts of dynamic shear moduli G' and G'' were measured as a function of ω immediately after N cycles of the large-amplitude oscillations where N was also varied.

III. Experimental Results

A. Structure at the Initial State before Shear Deformation. Figure 3 shows the DSC thermogram of SEP specimens used in this experiment in a temperature range near the glass transition of the PS microdomains. The thermogram obtained at a heating rate of 20 °C/min shows a change of the base line between 22 and 62 °C, reflecting the glass transition temperature T_g of the PS microdomains. The T_g of PEP is about −60 °C, well below the experimental temperature, so that PEP alone behaves like a liquid. Thus the PS microdomains are glassy spheres immersed in a liquid medium at the experimental temperature.

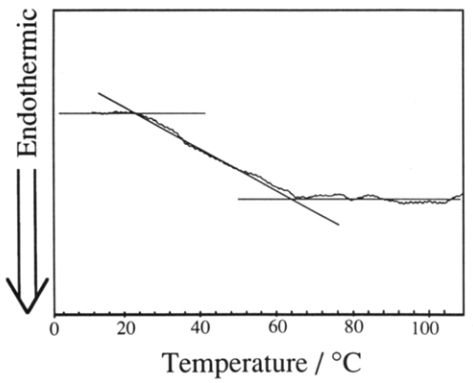

Figure 3. DSC thermogram obtained at a heating rate of 20 °C/min in a temperature range close to the glass transition temperature of the PS microdomains. The straight lines offer a visual guide for the thermogram.

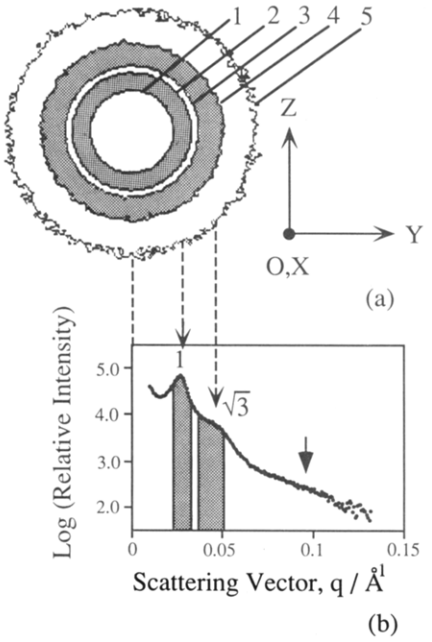

Figure 4. SAXS patterns taken by the 2D detector (a) and the circular-averaged intensity distribution with scattering vector q (b) for the undeformed SEP copolymer. The shaded zones in pattern a offer visual guides for the scattering maximum and shoulder. They also correspond to the intensity or q ranges shaded in part b. The contour lines numbered 1–5 in pattern a have logarithm of scattered intensity of 4.60, 4.24, 3.88, 3.52, and 3.16, respectively.

Figure 4 shows the 2D SAXS pattern taken with IP (part a) and the circular-averaged SAXS intensity distribution, $I(q)$, for the annealed specimens SEP (part b) where q is the scattering vector defined by $q = (4\pi/\lambda)\sin(\theta/2)$, θ being the scattering angle. The 2D pattern shows no azimuthal angle dependence. $I(q)$ shows a sharp first-order maximum at $q_m = 0.0297$ Å^{-1} and a shoulder at the position of about $3^{1/2}$ relative to the first-order maximum and a very broad maximum at $q \cong 0.1$ Å^{-1}, defined hereafter as $q_{m,p}$. The detailed analysis of $I(q)$ and transmission electron micrographs (TEM) yielded the following pieces of information:[12] (i) the spherical PS microdomains are dispersed in the matrix of PEP block chains, (ii) the first-order maximum and the higher order shoulder reflect the intersphere interference of the scattered waves, while the broad maximum at $q_{m,p}$ reflects the form factor of single spheres, and (iii) the number-average radius of the spheres $\bar{R}$ is 70.6 ± 0.25 Å, the standard deviation of the radius σ_R is 15.1 ± 0.35 Å, and the characteristic interfacial thickness $t_I = 13.3 \pm 0.9$ Å. The volume analysis yielded information that bcc is more favorable than the simple cubic lattice (sc) and the face-centered cubic lattice (fcc): the volume fraction of the PS spheres Φ_{PS} as calculated from the Bragg spacing $d = 2\pi/q_m = 212$ Å and $\bar{R}$ under the assumption of the bcc symmetry and that of a complete segregation of PS and PEP chains into the respective domains gives a best agreement with the volume fraction of the PS block chain in the copolymer ($f_{PS} = 0.1$). We obtained Φ_{PS} equal to 0.151 for sc, 0.107 for bcc, and 0.116 for fcc by using mass densities 1.06 and 0.86 g/cm^3 for PS and PEP, respectively. SAXS and TEM indicate that the lattice is considerably disordered and randomly oriented.

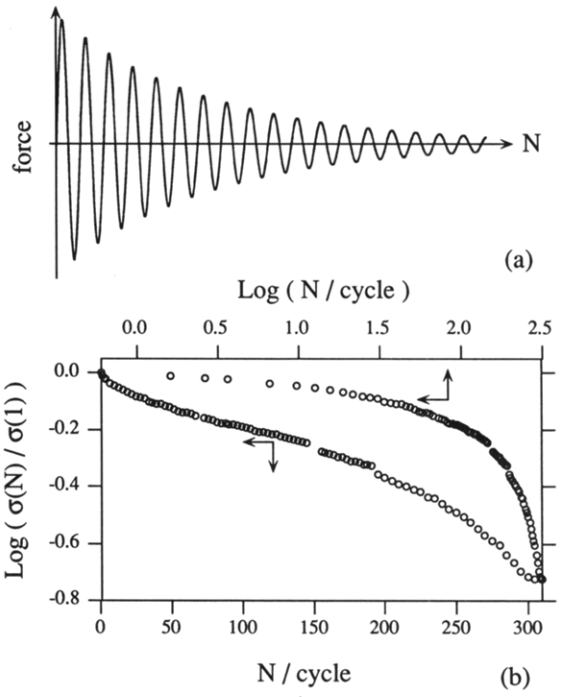

Figure 5. (a) Schematic diagram showing the variation of force under a large-amplitude oscillatory shear deformation, and (b) the decay of stress amplitude $\sigma(N)$ with a number of deformation cycles N relative to the stress amplitude at the first cycle of the deformation $\sigma(1)$.

B. Mechanical Properties. Upon imposing the large-amplitude oscillatory strain, the force detected by our transducer decayed as a function of N, as schematically shown in Figure 5a. The maximum stress for the Nth cycle of oscillation relative to that of the first cycle $\sigma(N)/\sigma(1)$ was plotted either semilogarithmically or double-logarithmically in Figure 5b. The stress decay appears to have at least two processes, i.e., the early and the late processes, which is believed to reflect a change of the microdomain structure of the system with N, as will be discussed later in section IV.

Figure 6 shows Lissajous figures for the large-amplitude oscillatory strain $\gamma_0 = 50\%$ (a) and for a relatively small strain $\gamma_0 = 17\%$ (b) at the same ω as described earlier. The data were obtained for the first cycle $N = 1$. The Lissajous figure in part a clearly shows nonlinear stress response as shown by the humps at two strain phases (marked by arrows), but the nonlinearity is less clear in part b. We noted that the nonlinearity seen in part a does not necessarily vanish when the stress $\sigma(N)$ decays with N.

Figure 7 shows the change of linear dynamic mechanical properties with N during the large-amplitude oscillatory deformation. The frequency dependence of the real part of the shear modulus G' and that of the imaginary part G'' are found nearly independent of N, and only their magnitudes decrease with N. The data for $N = 0$ stand for the data for the virgin sample. We also note the fact that at the low frequency of $\omega < 1$ the frequency

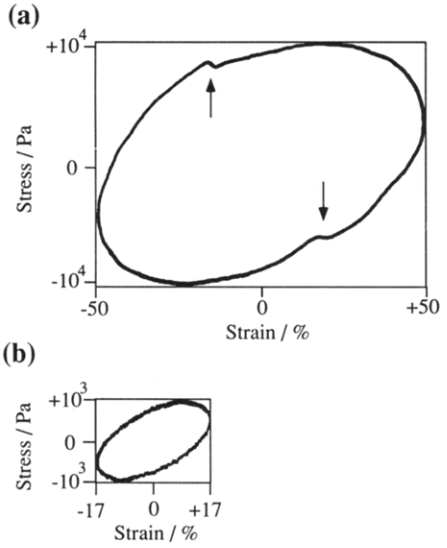

Figure 6. Typical Lissajous figures obtained for $\gamma_0 = 0.5$ (a) and $\gamma_0 = 0.17$ (b) in the first cycle of shear deformation at $\omega = 0.0936$ rad/s.

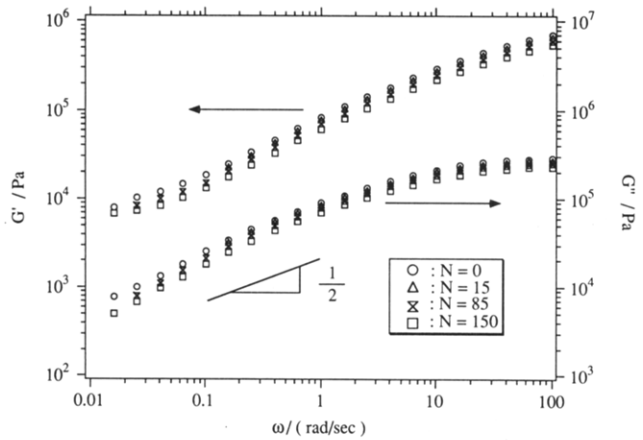

Figure 7. Linear dynamic mechanical properties obtained immediately after N cycles of the large-amplitude oscillatory shear deformation with varying N as shown in the figure. $N = 0$ corresponds to the results obtained with the virgin sample. G' and G'' are real and imaginary parts of the shear moduli, respectively.

dependence of G' is nearly identical to that of G'', i.e.

$$G', G'' \sim \omega^n \tag{1}$$

with $n \cong 0.6$. The low-frequency scaling behavior given by eq 1 seems typical of that of the ordered microdomain systems of block copolymers. The value $n \cong 0.5$ was reported for the lamellar phase.[13,14] The fact that the prefactor of ω^n depends on N is parallel to the fact that $\sigma(N)$ decays with N.

C. SAXS Results Obtained with the Average Mode. Figure 8a shows the SAXS patterns taken *in-situ* with IP during the large-amplitude oscillatory shear deformation. The pattern was taken with the average mode with $N = 30$ and $\Delta N = 150$. Comparing with the pattern in Figure 4a, we found that the shear deformation tends to preferentially orient a particular lattice plane. The diffraction pattern at the first-order maximum position, defined hereafter as $q_{m,l}$, is clearly directionally dependent: a sharp meridional two-point pattern along the Oz axis and long equatorial arcs along the Oy axis.

On the other hand, the SAXS intensity in the vicinity of $q_{m,p}$ is directionally independent, implying that the vitrified PS spheres are not deformed under the shear deformation. Thus, the bcc lattice is oriented and

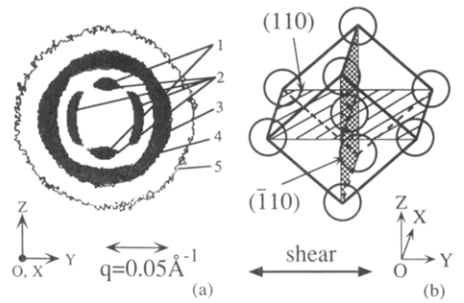

Figure 8. (a) SAXS pattern cumulated over the strain cycles defined by $N = 30$ and $\Delta N = 150$ (the average mode) during the large-amplitude oscillatory shear deformation and (b) the model showing a preferential orientation of the (110) lattice plane parallel to the Oxy plane. The shaded zones in pattern a offer visual guides for the scattering maximum and shoulder. The contour lines numbered 1–5 in pattern a have logarithm of scattered intensity of 4.66, 4.31, 3.64, 3.28, and 2.60, respectively.

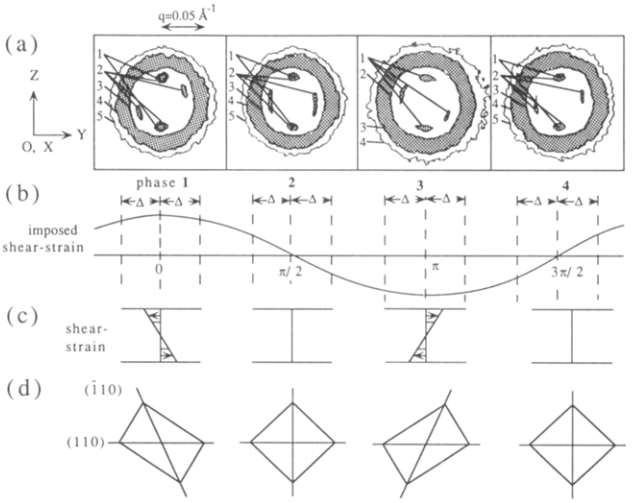

Figure 9. SAXS pattern (a) obtained at four representative strain phases as shown in b and c (the synchronous mode) and the model to explain the four diffraction spots arising from (110) and (1̄10) lattice planes (d). The pattern at each phase was obtained for the strain phase of $[-\Delta + \phi_i, \Delta + \phi_i]$ where $\phi_i = 0$, $\pi/2$, π, and $3\pi/2$ for phases 1–4, respectively, and $\Delta = 0.194\ \pi$. The pattern at each phase was obtained by cumulating the SAXS intensity over the strain cycles defined by $N = 80$ and $\Delta N = 70$. The shaded zones in pattern a offer visual guides for the scattering maximum and shoulder. The contour lines numbered 1–5 have respectively logarithm of scattering intensity of 3.60, 3.40, 2.80, 2.40, and 2.20 for the patterns in phases 1 and 2, 3.45, 2.77, 2.32, and 2.10 for those in phase 3, and 3.65, 3.42, 2.74, 2.28, and 2.05 for those in phase 4.

deformed, but the spheres remain undeformed under the shear deformation. Figure 8b presents a model showing preferred (110) plane orientation parallel to the Oxy plane to explain the two-point pattern observed under the oscillatory shear deformation. The details will be discussed later in section IV. Our preliminary results indicated that the meridional two-point pattern shown in part a becomes increasingly sharp with N, although not shown here.

D. SAXS Results Obtained with the Synchronous Mode. In order to gain a deeper insight into the lattice deformation and orientation under the shear deformation, the SAXS pattern was taken *in-situ* with the *synchronous mode* and with $N = 80$ and $\Delta N = 70$. The patterns in Figure 9a were taken at four representative strain phases centered at 0, $\pi/2$, π, and $3\pi/2$ (designated phases 1–4, respectively) and over the phase interval $2\Delta = 0.388\pi$, as shown in parts b and c. The response of the pattern at the $q_{m,l}$ position is particularly interesting: each pattern in part a is composed of four points. The two points along the Oz axis are almost stationary, staying parallel to the

Oz axis for all the strain phases, but the other two points are oscillating; i.e., they are approximately at 65°, 90°, 115°, and 90° with respect to the *Oz* axis in phases 1–4, respectively. Part d indicates a qualitative, simplified model to explain the above observation, the details of which will be discussed in section IV.

IV. Discussion

A. Response of the bcc Lattice. The results obtained in Figure 9a clarify the pattern obtained in Figure 8a. The meridional two-point pattern along the *Oz* axis should arise from the (110) plane oriented more or less stationarily parallel to the plane *Oxy*, as shown in Figures 8b and 9d, while the other two-point pattern (equatorial two-point pattern) changes its orientation, oscillating in the *Oyz* plane about the equator with a change of the strain phase, as shown in Figure 9a. Hence, in the average mode, the oscillating equatorial two-point pattern should appear to be a long arc, while the stationary meridional two-point pattern should remain two-point like, as shown in Figure 8a. The oscillating equatorial two-point patterns in Figure 9a or the long equatorial arc in Figure 8a should arise from the ($\bar{1}10$) plane orthogonal to the (110) plane. The oscillating pattern indicates a dynamic lattice deformation as shown schematically in Figure 9d.

Thus, the results obtained in Figures 8 and 9 immediately give us the following two conclusions. (1) Under the oscillatory shear deformation, the (110) plane having the highest number density of the spheres orients parallel to the *Oxy* plane. A similar orientation of the (110) plane parallel to the *Oxy* plane was also reported after cessation of a large-amplitude oscillatory shear strain.[4] We found that the degree of orientation of the (110) plane increases with N. Our preliminary SAXS results with the average mode indicate that a rapid increase in the degree of orientation is achieved for the first 30 cycles and a further increase of the orientation occurs gradually with a further increase of N. (2) In response to the applied shear deformation, the bcc lattice undergoes dynamic lattice deformation under the constraint that the (110) planes orient, by and large, parallel to the *Oxy* plane. The position of the meridional two-point pattern with respect to θ or q remains almost unchanged with the strain phase, indicating that the (110) spacing is essentially kept constant during the deformation. However, the position of the ($\bar{1}10$) diffraction peak changes with the strain phase: the positions of the diagonal two-point pattern in phases 1 and 3 locate at higher q than those of the equatorial two-point pattern in phases 2 and 4. The latter positions locate at smaller q than those of the meridional two-point pattern. The change of ($\bar{1}10$) diffraction spots with the strain phase implies the ($\bar{1}10$) spacing is stretched under the shear deformation in phases 2 and 4 and that it tends to be compressed in phases 1 and 3. We roughly estimated the strain amplitude imposed on the crystal γ_{cryst} from the changes of (110) and ($\bar{1}10$) with the strain to be $\gamma_{cryst} \cong \tan 25° = 0.47$, close to γ_0, where the angle 25° is that between the equator and the line connecting the centers of the diagonal two-point patterns in phases 1 and 3.

Close observations of the results in Figure 9a lead us to the following additional conclusions. (3) If the crystal deformation as indicated in Figure 9d occurs in phase with the applied strain phase, the SAXS patterns obtained in phases 2 and 4 should be identical and those obtained in phases 1 and 3 should be in mirror-image with respect to the *Oz* axis. However, the patterns in phases 2 and 4 are not clearly identical, indicating that a phase difference exists between the applied strain and the strain on the crystal. (4) The width of the meridional two-point pattern along the azimuthal-angular direction appears to depend on the strain phase. This implies a dynamic variation of the crystal orientation as a whole under the oscillatory deformation. (5) Our preliminary SAXS results with the synchronous mode with a small fixed ΔN but varying N appear to indicate that the lattice strain γ_{cryst} gradually decreases with N in the region of $N > 40$.

B. Origin of Stress Decay. Conclusions 1–5 obtained in section IV-A should be somehow related to the rheological behavior of the systems under the large-amplitude oscillatory shear strain (Figure 5) as well as under the small strain (Figure 7). The rheological behavior should be affected by all the factors given above; the orientation of the (110) plane (conclusion 1), the dynamic deformation of the bcc lattice (conclusion 2), its loss tangent (conclusion 3) and their changes with N (conclusion 5), and the dynamic orientation of the crystal as a whole (conclusion 4).

The decay of the stress amplitude $\sigma(N)$ with N appears to be apparently composed of the early and the late processes which dominate at $N \ll 30$ and $N \gg 30$, respectively. The rapid orientation of the (110) plane parallel to the *Oxy* plane (conclusion 1) is apparently related to the decay process in the early stage, while the gradual decrease of the lattice deformation γ_{cryst} with N (conclusion 5) is related to the decay process in the late stage. The phase difference of the lattice deformation and orientation against the strain (conclusion 3) may be related to the large loss tangent observed in the Lissajous figures in Figure 6.

The decrease of the dynamic lattice strain γ_{cryst} with N may occur as a consequence of increased volume fraction of the grain-boundary region where the cubic packing of the spheres may be more disordered than that inside the grain. This effect may account also for the decrease of G' and G'' with N in Figure 7.

C. Relaxation after Cessation of Oscillatory Shear. The orientation of the (110) plane developed under the large-amplitude oscillatory shear deformation was found to relax into random orientation after cessation of the shear, as shown in Figure 10 where the pattern in part a was obtained during the oscillatory shear deformation with the average mode and with $N = 30$ and $\Delta N = 150$. The pattern in part b was taken from 0 to 1000 s after the cessation of the shear deformation. Patterns a and b have the azimuthal-anglar dependence of the first-order diffraction intensity as shown in curves I and II in part c, respectively. This clearly indicates the orientational memory built up by the shear deformation completely decays after the cessation. This fact is a big surprise to us, puzzling but yet intriguing. It is also a big contrast to the results reported by Almdal et al.[4] They reported a high orientation of the bcc lattice even after cessation of the shear at zero strain. Interestingly decay of the orientation memory causes the recovery of stress after the cessation of the shear as is demonstrated in Figure 11.

The virgin sample shows the stress decay with N during the large-amplitude oscillatory deformation as shown in the curve labeled 1 in Figure 11. After oscillation up to $N = 300$, the stress decayed to point A. In this figure $\sigma(1)$ always refers to the stress at $N = 1$ for the virgin sample. The specimen subjected to oscillation up to $N \cong 300$ was released from the strain and left relaxed for 4.5 h at room temperature. The stress at point A was relaxed to zero (point B) after release of the strain to zero. After the rest for 4.5 h at room temperature, the large-amplitude shear deformation was applied again to the specimen, and the stress decay was measured as a function of N. The result is shown by the curve labeled 2. We found the stress recovery to point C at the second-run deformation, which

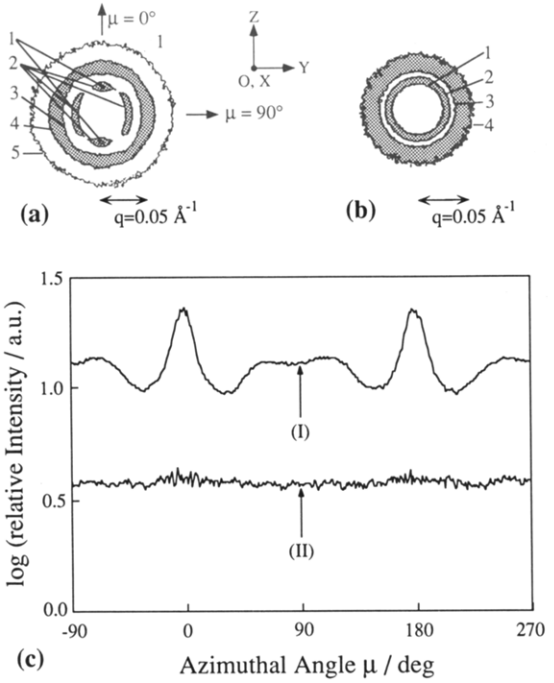

Figure 10. Change of the SAXS pattern with time after cessation of the large-amplitude oscillatory shear deformation. Pattern a was obtained during oscillatory shear deformation with the average mode with $N = 30$ and $\Delta N = 150$. After this experiment, the shear deformation was stopped at zero strain. Then pattern b was taken from 0 to 1000 s after cessation of the shear deformation. The azimuthal-anglar dependences for the first-order diffraction maximum in patterns a and b are shown by curves I and II, respectively, in part c. The shaded zones of patterns a and b offer visual guides for the scattering maximum and shoulder. The contour lines numbered 1–5 for pattern a have respectively logarithm of scattered intensity of 4.66, 4.31, 3.64, 3.28, and 2.60, while those numbered 1–4 for pattern b have respectively 2.81, 2.61, 2.27, and 2.03.

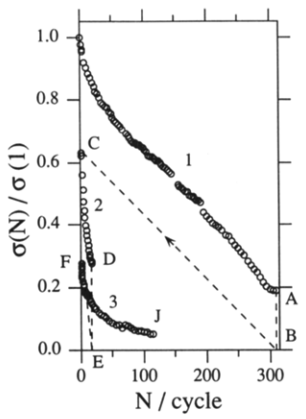

Figure 11. Stress recovery after cessation of the large-amplitude oscillatory shear strain. The decay of the stress amplitude $\sigma(N)/\sigma(1)$ with N under the deformation was plotted for the virgin sample (curve 1), for the sample subjected to the first-run deformation to point A and then relaxed to zero strain for 4.5 h (curve 2) and for the sample subjected to the second-run deformation to point D and then relaxed to zero strain for a few minutes (curve 3). $\sigma(1)$ always refers to the maximum stress at the first cycle of the deformation for the virgin sample.

may be due to a structure recovery during the rest. The stress decay due to the oscillation (point C to point D) is found to be much faster in the second run than in the first run. The same specimen was released from the strain at point D, and the stress relaxation occurred to point E. The specimen was left at room temperature for 2–3 m and then subjected to the third-run oscillatory deformation. The stress decay is shown by the curve labeled 3. It is clearly seen that the amount of stress recovery depends on the time spent for the stress relaxation. Almost no stress recovery is attained during the relaxation between the second and the third runs; i.e., the stress level of point D is almost the same as that of point F. The initial stress decay with N appears to increase in the order of the first run, the second run, and the third run. However, the stress decay rate appears to be slowed down as the stress level decreases, which is obvious in curve 3.

The recovery of the stress may be attributed to a recovery of the cubic structure in the grain-boundary region in which the bcc crystallike structure may be transformed into the spheres packed in the disordered lattice under the large-amplitude oscillatory strain. The recovery of the lattice structure in the grain boundary may induce disorientation and reorganization of the shear-aligned lattice structure in the strong segregation limit, resulting in the relaxation of the structure and stress recovery after cessation of the shear deformation.

V. Concluding Remarks

In this work we presented a structural response of the spherical microdomains of block copolymers to a large-amplitude oscillatory shear deformation in the regime of low-temperature and strong-segregation limit. The regime explored is quite different from the high-temperature and weak-segregation regime covered by previous work, e.g., Almdal et al.[4] The information obtained covers not only the structure attained after cessation but also *real time, in-situ* response of the domains which has not been reported previously. The high-temperature and weak-segregation system contains the soft spheres in the soft matrix near the order–disorder transition (ODT), while the low-temperature and strong segregation system contains the vitrified hard spheres in the soft matrix far below ODT. Thus, the former system should be subjected to structure reorganization under shear more easily and extensively than the latter system. We hope that our information obtained with the low-temperature behavior is also important to the enrichment of our understanding of the rheo-optical behavior of block copolymers. A more detailed analysis and theoretical interpretation of our results deserve future work.

References and Notes

(1) Hashimoto, T.; Shibayama, M.; Kawai, H.; Watanabe, H.; Kotaka, T. *Macromolecules* **1983**, *16*, 361.
(2) Hosemann, R.; Bagchi, S. N. *Direct Analysis of Diffraction by Matter*; North-Holland: Amsterdam, The Netherlands, 1962.
(3) Matsuoka, H.; Tanaka, H.; Hashimoto, T.; Ise, N. *Phys. Rev.* **1987**, *B36*, 1754. Matsuoka, H.; Tanaka, H.; Iizuka, N.; Hashimoto, T.; Ise, N. *Phys. Rev.* **1990**, *B41*, 3854.
(4) Almdal, K.; Koppi, K. A.; Bates, F. S. *Macromolecules* **1993**, *26*, 4058 and references cited therein.
(5) Kawamura, T.; Hashimoto, T., unpublished data.
(6) Ohta, T.; Enomoto, Y.; Harden, J. L.; Doi, M. *Macromolecules* **1993**, *26*, 4928.
(7) Doi, M.; Harden, J. L.; Ohta, T. *Macromolecules* **1993**, *26*, 4935.
(8) Phoon, C. L.; Higgins, J. S.; Allegra, G.; van Leeuwen, P.; Staples, E. *Proc. R. Soc. London A* **1993**, *442*, 221.
(9) Hashimoto, T.; Suehiro, S.; Shibayama, M.; Saijo, K.; Kawai, H. *Polym. J.* **1981**, *13*, 501. Hashimoto, T.; Saijo, K.; Kość, M.; Kawai, H.; Wasiak, A.; Ziabicki, A. *Macromolecules* **1985**, *18*, 472.
(10) Suehiro, S.; Saijo, K.; Ohta, Y.; Hashimoto, T.; Kawai, H. *Anal. Chim. Acta* **1986**, *189*, 41.
(11) Hashimoto, T.; Kume, T.; Saijo, K.; Kimishima, K.; Okamoto, S., in preparation.
(12) Hashimoto, T.; Kawamura, T.; Harada, M.; Tanaka, H. *Macromolecules* **1994**, *27*, 3063.
(13) Bates, F. S. *Macromolecules* **1984**, *17*, 2607. Rosedale, J. H.; Bates, F. S. *Macromolecules* **1990**, *23*, 2329. Koppi, K. A.; Tirrel, M.; Bates, F. S.; Almdal, K.; Colby, R. H. *J. Phys. II (Fr.)* **1992**, *2*, 1941.
(14) Kawasaki, K.; Onuki, A. *Phys. Rev.* **1990**, *A42*, 3664.